A MODEL-BASED APPROACH TO THE COMMON-DIFFRACTION-SURFACE STACK

H. Shahsavani and J. Mann

email: *shahsavani@shahroodut.ac.ir*

keywords: *stacking, ray tracing, common reflection surface, common diffrcation surface*

ABSTRACT

The Common-Reflection-Surface stack method parameterizes and stacks seismic reflection events in a generalized stacking velocity analysis. The implementation is able to deal with a discrete number of events contributing to a given stack sample such that conflicting dip situations can be handled. However, the reliable detection of such situations is difficult and missed contributions to the stacked section might cause artifacts in a subsequent poststack migration. This is deleterious for complex data where prestack migration is no viable option due to its requirements concerning the accuracy of the velocity model, such that we might have to rely on poststack migration. In addition to the handling of a small number of discrete dips, the conflicting dip problem has been addressed by explicitely considering a virtually continuous range of dips with a simplified Common-Reflection-Surface stack operator in a process termed Common-Diffraction-Surface stack. In analogy to the Common-Reflection-Surface stack, the Common-Diffraction-Surface stack has been implemented and successfully applied in a data-driven manner. As this comes along with significant computational costs, we now present a much more efficient model-based approach to the Common-Diffraction-Surface stack which is designed to generate complete stack sections optimized for poststack migration. This approach only requires a smooth macro-velocity model of minor accuracy. We present first preliminary results for a real land data set.

INTRODUCTION

For more than a decade, the Common-Reflection-Surface (CRS) stack method has been extensively discussed in the annual WIT reports and in various publications. Therefore, we will here restrict the discussion of the CRS method to the very basic essentials required in the scope of this contribution: the CRS method follows the concept of the classical stacking velocity analysis, the local parameterization and stacking of reflection events by means of an analytic second-order approximation of the reflection traveltime (see, e. g., Mann et al., 1999; Jäger et al., 2001). Conventional stacking velocity analysis is applied within individual common-midpoint (CMP) gathers with the stacking velocity as the only stacking parameter (in general azimuth-dependent in 3D). In contrast, the CRS approach also takes neighboring CMP gathers in account, acknowledging the fact that reflection events are caused by spatially contiguous reflector elements in depth. The relation between conventional stacking velocity analysis and the CRS approach has been described by Hertweck et al. (2007) in terms of horizontal slowness and two imaging velocities to highlight the similarities between these approaches. Equivalent formulations can be given in terms of spatial traveltime derivatives or in terms of properties of hypothetical wavefronts, namely the emergence direction of the normal ray connecting the reflection point to the surface and the curvatures of wavefronts associated with a point source at the reflection point or a exploding reflector segment around the latter, respectively. For the sake of consistence with related publications, we will use the latter description in the following.

In its simplest implementation, the CRS stack determines only one optimum stacking operator for each zero-offset (ZO) sample to be simulated. Along this operator, we obtain the maximum coherence in the

seismic reflection data. This works nicely if there is only one reflection event contributing to the considered sample or no coherent event at all. However, in the presence of curved reflectors or diffractors, various events might intersect each other and/or themselves, such that a single stacking operator per ZO sample is no longer appropriate to completely simulate a stacked section. To account for such situations, Mann (2001, 2002) proposed to allow for a small, discrete number of multiple stacking operators for a particular ZO sample. The main difficulty in this approach is to identify conflicting dip situations and to decide how many contributions should be considered. This implies a tricky balancing between lacking contributions and potential artifacts due to the unwanted parameterization of spurious events. Due to the discrete number of considered events, the number of detected and, thus, imaged events might change from sample to sample such that seismic events might still show up in fragments, only.

The introduction of inversion methods fully exploiting the information contained in the CRS stacking parameters (Duveneck, 2004a,b) enabled a consistent imaging workflow consisting of CRS stack, normal-incidence-point (NIP) wave tomography, and prestack depth migration (see, e. g., Mann et al., 2003; Heilmann et al., 2004; Hertweck et al., 2004). In this workflow, the stacked section mainly serves as an intermediate result for picking rather than as a final image for interpretation. Thus, lacking contributions in the stacked section due to conflicting dip situations are acceptable and do not affect the final depth image. However, in data of complex nature and/or high noise level, generating a macro-velocity model of sufficient accuracy for prestack depth migration might not be feasible with reasonable effort. In such cases, poststack migration with its much lower requirements in velocity model accuracy is more attractive—and the completeness of the stacked section turns into a relevant issue again.

Soleimani et al. (2009b,a) proposed an adapted CRS strategy designed to obtain a stacked section as completely as possible by merging concepts of the dip moveout (DMO) correction (e. g., Hale, 1991) with the CRS approach: instead of only allowing a single stacking operator or a small discrete number of stacking operators per sample, a virtually continuous range of dips is considered. To simplify this process and to further emphasize usually weak diffraction events, this has been implemented with a CRS operator reduced to (hypothetical) diffraction events. This so-called Common-Diffraction-Surface (CDS) stack approach has been successfully applied to complex land data (Soleimani et al., 2010). However, the approach is quite time consuming, as separate stacking operators have to be determined for each stacked sample to be simulated and each considered dip in a data-driven manner by means of coherence analysis in the prestack data.

Here, we propose a model-based approach to the CDS stack. We assume that a smooth macro-velocity model has already been determined, e. g. by means of CRS stack plus NIP-wave tomography. Under this conditions, the parameters of the CDS stacking operators can be easily forward-modeled by means of kinematic and dynamic ray tracing. In this way, a complete stacked section optimized for poststack depth migration can be generated in a much more efficient manner compared to the data-driven CDS approach.

TRAVELTIME APPROXIMATION

The CRS method is based on an analytical approximation of the reflection traveltime up to second order in terms of the half source/receiver offset h and the displacement of the source/receiver midpoint x_m with respect to the location x_0 of the stacked trace to be simulated. This approximation can be expressed in different flavors, e. g. in a parametric form or in Taylor series expansions in terms of traveltime or squared traveltime, respectively (Höcht et al., 1999). The most popular form is the hyperbolic traveltime expansion, as it directly resembles the well-known common-midpoint (CMP) traveltime approximation for $x_m = x_0$. For the 2D case considered in this paper, the hyperbolic CRS traveltime approximation can be expressed as

$$t^2\left(x_m, h\right) = \left[t_0 + \frac{2\sin\alpha}{v_0}\left(x_m - x_0\right)\right]^2 + \frac{2t_0\cos^2\alpha}{v_0}\left[\frac{\left(x_m - x_0\right)^2}{R_{\mathrm{N}}} + \frac{h^2}{R_{\mathrm{NIP}}}\right], \tag{1}$$

with v_0 denoting the near-surface velocity. The stacking parameter α is the emergence angle of the normal ray, whereas R_{N} and R_{NIP} are the local radii of hypothetical wavefronts excited by a exploding reflector experiment or a exploding point source at the (unknown) reflection point of the normal ray, the normal incidence point (NIP). All these properties are defined at $(x_0, z = 0)$.

For a true diffractor in the subsurface, an exploding point source experiment and an exploding reflector experiment naturally coincide such that $R_{\mathrm{NIP}} \equiv R_{\mathrm{N}}$. Thus, for *diffraction* events, the CRS traveltime

equation (1) reduces to the CDS traveltime approximation

$$t^2\left(x_m,h\right)=\left[t_0+\frac{2\sin\alpha}{v_0}\left(x_m-x_0\right)\right]^2+\frac{2t_0\cos^2\alpha}{v_0\,R_{\mathrm{CDS}}}\left[\left(x_m-x_0\right)^2+h^2\right]\,, \tag{2}$$

with $R_{\mathrm{CDS}}\equiv R_{\mathrm{NIP}}\equiv R_{\mathrm{N}}$. For *reflection* events, the CDS operator (2) is an inferior approximation compared to the full CRS operator (1) as $R_{\mathrm{NIP}}\neq R_{\mathrm{N}}$. Nevertheless, it still allows to approximate the event within a reasonably chosen aperture. For the data-driven CDS stack, this simplified operator has been chosen for performance reasons. For the model-based CDS stack, this simplification is mandatory, as there is no structural information on reflector curvatures contained in the considered smooth macro-velocity model. Thus, a forward-modeling of the lacking parameter R_{N} is not possible anyway.

Note that the meaning of R_{CDS} depends on the way this stacking parameter is determined: in the forward-modeling discussed below, it is a completely local second-order property $R_{\mathrm{NIP,mod}}$ of the emerging NIP wavefront at the considered ZO location. In the CRS stack, the second-order property $R_{\mathrm{NIP,data}}$ is determined from the prestack data within a finite aperture. Thus, $R_{\mathrm{NIP,data}}$ is, in general, subject to spread length bias and does not exactly coincide with the forward-modeled $R_{\mathrm{NIP,mod}}$ (Müller, 2006). In the data-based CDS stack, R_{CDS} is influenced by both data-derived attributes $R_{\mathrm{NIP,data}}$ and $R_{\mathrm{N,data}}$. It represents a kind of weighted average of these both attributes, depending on the aspect ratio of the used aperture. In the context of this paper, we consider the forward-modeled case, i. e., $R_{\mathrm{CDS}}\equiv R_{\mathrm{NIP,mod}}$.

FORWARD-MODELING

As already mentioned above, the radius of the NIP wave occurring in the CDS operator (2) is associated with a hypothetical point source at the NIP. The local curvature of the hypothetical wavefront triggered by such a point source is considered along the normal ray. The wavefront finally reaches the acquisition surface with the curvature $1/R_{\mathrm{NIP}}$. Thus, the first step to model this parameter is to determine the potential normal ray by means of kinematic ray tracing. As we need this ray for a given surface location and a given emergence angle, the kinematic ray tracing is performed for the down-going ray.

Kinematic ray tracing consists in the calculation of the characteristics of the Eikonal equation

$$\left(\nabla T\right)^2=\frac{1}{v^2\left(x,z\right)}\,, \tag{3}$$

which governs the kinematics of the wavefield in a 2D velocity field $v\left(x,z\right)$. In the following, we will use the Einstein summation convention for the sake of briefness. According to Červený (2001), the Eikonal equation's characteristics

$$\frac{dx_i}{du}=\frac{\partial\mathcal{H}}{\partial p_i}\,,\quad \frac{dp_i}{du}=-\frac{\partial\mathcal{H}}{\partial x_i}\,,\quad \frac{dT}{du}=p_k\frac{\partial\mathcal{H}}{\partial p_k}\quad;\quad i=1,2 \tag{4}$$

are defined in a generalized domain consisting of slowness vector $\vec{p}$ and spatial coordinates $\vec{x}$. The projection of these characteristics into the space domain represents the searched-for ray paths. A general form of the Hamiltonian is

$$\mathcal{H}\left(\vec{x},\vec{p}\right)=n^{-1}\left[\left(p_i\,p_i\right)^{\frac{n}{2}}-v^{-n}\right]=0\quad;\quad i=1,2\,, \tag{5}$$

with n as a real number. For reasons which will become evident below, we will here use the limit of $n\rightarrow 0$ which yields the Hamiltonian

$$\mathcal{H}\left(\vec{x},\vec{p}\right)=\frac{1}{2}\ln\left(p_i\,p_i\right)+\ln v=\frac{1}{2}\ln\left(v^2p_i\,p_i\right)\,. \tag{6}$$

For this case, the last characteristic in equation (4) reduces to $dT/du=1$, i. e., the variable u along the ray is directly the traveltime. This is a desired feature, as we have to compute ray tracing results for a regular grid in ZO traveltime.

The corresponding kinematic ray tracing system, a system of four coupled ordinary differential equations, reads

$$\frac{dx_i}{dT}=\left(p_k\,p_k\right)^{-1}p_i\quad\frac{dp_i}{dT}=-\frac{\partial\ln v}{\partial x_i}\quad;\quad i=1,2 \tag{7}$$

and can be numerically integrated with the well known Runge-Kutta scheme of fourth order. The step length in the numerical solution is chosen as an integer fraction of the sampling rate of the stacked section to be simulated. In this way, we directly obtain the discrete points along the ray paths corresponding to the desired output locations in the ZO time domain.

As $|\vec{p}| \equiv 1/v(x,z) \ \forall \ \vec{x}$, the slowness components are not independent of each other such that the system of equations can be further reduced. However, using Cartesian coordinates, the reduced system is not able to handle turning rays. Therefore, we use the full system of equations and enforce the relation between slowness and velocity by an according rescaling of $\vec{p}$ after each ray tracing step.[1]

The determination of R_{NIP} additionally requires dynamic ray tracing along the ray path. The derivation of the dynamic ray tracing system again starts with the Eikonal equation, now defined in ray-centered coordinates (s,n), with s being the coordinate tangent to the ray and n the coordinate normal to the ray. A Taylor expansion of the phase function T in the vicinity of the central ray introduces the second partial derivative M of the traveltime normal to the central ray:

$$M(u) = \left.\frac{\partial^2 T(u,n)}{\partial n^2}\right|_{n=0} . \tag{8}$$

The resulting ordinary differential equation of Ricatti type finally yields the dynamic ray tracing system consisting of two coupled ordinary differential equations of first order. For our chosen propagation variable $u \equiv t$ along the central ray, this system reads

$$\frac{dq}{dt} = v^2 p\,, \quad \frac{dp}{dt} = -\frac{1}{v}\frac{\partial^2 v}{\partial n^2} q\,, \tag{9}$$

which can be easily numerically integrated along the ray in parallel to the kinematic ray tracing described above. The properties p and q are related to different coordinate transforms, see Červený (2001) for details. The only important property here is that their ratio coincides with the the second traveltime derivative normal to the ray, equation (8):

$$M(u) = \frac{p(u)}{q(u)}\,. \tag{10}$$

In turn, for a point source at the NIP, $M(u_0)$ at the emergence point of the normal ray is directly related to the searched-for value of R_{CDS}:

$$\frac{1}{R_{\text{CDS}}} = v_0 M(u_0) = v_0 \frac{p(u_0)}{q(u_0)}\,, \tag{11}$$

with v_0 again representing the near-surface velocity at the emergence point.

A straightforward approach to this task is to integrate the dynamic ray tracing system upwards along the ray for a given point on the known down-going ray path with the according initial condition for a point source initial condition in the starting point, i. e., $q = 0$ and $p = 1$. However, this approach is highly inefficient for two reasons:

- dynamic ray tracing had to be performed separately for each considered point on the ray, i. e., hundreds or thousands of times along each ray
- either the entire down-going ray paths had to be kept in memory, or kinematic ray tracing has to be repeated along the up-going ray path again

Instead, it is far more efficient to perform the dynamic ray tracing in parallel to the kinematic ray tracing along the down-going ray. However, in this way we cannot directly control the desired "initial" condition at the NIPs, because now the initial conditions are defined at the acquisition surface rather than at the NIPs. Fortunately, this problem can be addressed by solving the dynamic ray tracing system for two mutually orthogonal initial conditions, a point source and a plane wave at the initial point. The initial condition for

[1] Due to numerical inaccuracies, $|\vec{p}|$ slowly starts to deviate from $1/v\,(x,z)$ with increasing length of the ray path which would violate the Eikonal equation (3).

the latter reads $q = 1$ and $p = 0$. Using the index 2 for the point source initial condition and index 1 for the plane wave initial condition, the solutions can be gathered in a ray propagator matrix $\mathbf{\Pi}$:

$$\mathbf{\Pi}\left(u;u_0\right) = \begin{pmatrix} q_1 & q_2 \\ p_1 & p_2 \end{pmatrix}. \tag{12}$$

This ray propagator matrix can be computed along the ray for any value of u along the ray with the two initial conditions being defined at the emergence location of the central ray associated with u_0.

One of the powerful features of the ray propagator matrix $\mathbf{\Pi}(u;u_0)$ is that it can be easily converted into the corresponding propagator matrix $\mathbf{\Pi}^b(u_0;u)$ describing the dynamic properties in opposite propagation direction along the ray:

$$\mathbf{\Pi}^b\left(u_0;u\right) = \begin{pmatrix} p_2 & q_2 \\ p_1 & q_1 \end{pmatrix}. \tag{13}$$

The first column of $\mathbf{\Pi}^b$ again corresponds to the plane wave initial conditions and the second column to the point source initial conditions, but these initial conditions are now defined at the considered point u on the central ray. As we compute $\mathbf{\Pi}$ along the down-going ray for all required locations u on the ray, $\mathbf{\Pi}^b$ is readily available, too. Its second column exactly describes the desired situation: the solution of the dynamic ray tracing system at the emergence point of the central ray for a point source initial condition at any considered point u along the ray! Thus, the searched-for stacking parameters are simply given by

$$\frac{1}{R_{\mathrm{CDS}}(u)} = v_0 \frac{q_2(u)}{q_1(u)}. \tag{14}$$

IMPLEMENTATION

The existing 2D implementation of the CRS stack has been extended to allow for a model-based calculation of stacking parameters. In addition to a new class which actually performs the stacking process, two additional classes have been added: the first one provides the velocity model and various of its spatial derivatives interpolated to any required depth location, the second one implements the kinematic and dynamic ray tracing systems and provides the CDS stacking parameter directly on the ZO target grid. Symbolically and omitting all I/O issues, the algorithm can be summarized as follows:

```
set up velocity model & derivatives
for each ZO trace {
  for each emergence angle on coarse grid {
    trace ray up to maximum ZO time
    calculate stacking parameters for all ZO samples
  }
  for each ZO sample {
    for each emergence angle on fine grid {
      interpolate stacking parameter between nearest rays
      stack along CDS operator
      calculate semblance along CDS operator
      keep track of contribution with highest semblance
    }
    weighted/thresholded superposition of individual stack results
  }
}
```

The implementation relies on all the existing classes for I/O, stacking, semblance calculation, aperture handling etc., just as the data-driven counterparts. The model-based CDS algorithm is very efficient, as the ray tracing is performed only once per ZO trace and emergence angle, rather than within the innermost loop. In view of the fact that the stacking parameter varies smoothly for a smooth velocity model, the rays can be calculated on a relatively coarse emergence angle grid. In contrast, the semblance and the stack itself are quite sensitive to variations of the emergence angle. Thus, stack and semblance are calculated on a finer emergence angle grid using interpolated stacking parameters.

The implemented ray tracing system generally supports turning rays such that e. g. overhanging flanks can be imaged. Depending on the complexity of the considered data, the user can decide whether turning rays should be further traced or simply terminated at their turning points. The latter option significantly speeds up the code, as many CDS operators unlikely to actually contribute to the image will not be evaluated at all. This especially applies to large ZO traveltimes combined with large emergence angles.

Although the stacking parameters do not have to be optimized as in the data-driven approaches, it turned out to be quite useful to calculate semblance along the individual CDS operators anyway. Note that this has to be performed only once per emergence angle for each ZO sample rather than dozens or hundreds of times as in the data-driven CDS stack. Thus, the semblance calculation is not a performance issue in the model-based case but enables several additional features:

- We can keep track of the CDS operator yielding the highest semblance.[2] In this way we can obtain
  - a section of the highest encountered semblance,
  - a section with the corresponding emergence angle α, and
  - a section with the corresponding radius of curvature R_{CDS}.

  Obviously, these sections resemble the coherence section, the emergence angle section, and the R_{NIP} section of the data-driven CRS stack to some extent. Thus, they allow for the identification of ZO reflection events, the assessment of the quality of the operator fit, and plausibility analyses.
- The semblance associated with a particular CDS operator can be used as a weight factor for its contribution to the final stack section, probably in combination with a semblance threshold. This allows to reduce the overall noise level and is subject of our current investigations.

FIRST RESULTS

For the first application of the newly implemented model-based CDS stack, we revisited the 2D land data set presented by Soleimani et al. (2009a) in the context of the data-driven CDS stack. The line acquired by an energy resource company in fixed-spread geometry has a length of about $12\,\mathrm{km}$, $50\,\mathrm{m}$ shot and receiver spacing and a temporal sampling rate of $2\,\mathrm{ms}$. For further details on source signals and preprocessing, we refer to Soleimani et al. (2009a).

A sequence of CRS stack and NIP-wave inversion has been applied to the data to obtain the smooth macro-velocity model shown in Figure 1. This CRS-based imaging workflow has, e. g., been extensively discussed by Mann et al. (2003) and Hertweck et al. (2004) such that there is no need to go into any details here. During the model-based CDS stack, kinematic and dynamic ray tracing is performed in this model for a coarse emergence angle grid ranging from -22° to 22° in steps of 2°. The corresponding ray fan for one of the ZO trace locations is superimposed on the model in Figure 1. Due to the chosen parameterization of the kinematic ray tracing system, the stacking parameters R_{CDS} are directly available on the temporal target grid without the need for any interpolation along the rays. For the stack and the semblance calculation, we used a finer emergence angle grid ranging from -20° to 20° in steps of 1° with stacking parameters linearly interpolated in between neighboring rays on the coarse grid.

In Figure 2, the stacked sections obtained with the different approaches are compiled for comparison. Figure 2a shows the final result of the CRS stack, the stack confined to the first projected Fresnel zone after local three-parameter optimization (see, e. g., Mann, 2002) and event-consistent smoothing (Hertweck et al., 2005) of the CRS attributes. The reflection events show up with a high signal-to-noise ratio and high continuity. However, many events are truncated and only appear in fragments where they intersect more dominant events. Evidently, this will lead to artifacts in a subsequent poststack migration. Especially faults will be poorly imaged, as the corresponding edge diffraction are largely missing in the stacked section. In the data-driven CDS-stacked section in Figure 2b, these conflicting dip situations are fully resolved and the interference of intersecting events is properly simulated and many new steep events show up. Compared to

[2] An CDS operator with higher semblance is only accepted as supremum if the number of contributing traces is not lower than for any other operator for the same ZO sample. This prevents e. g. very steep operators from being selected for such suprema. Semblance will generally increase with decreasing number of contributing traces, which renders the semblance values incomparable and obscures the actual quality of the operator fit.

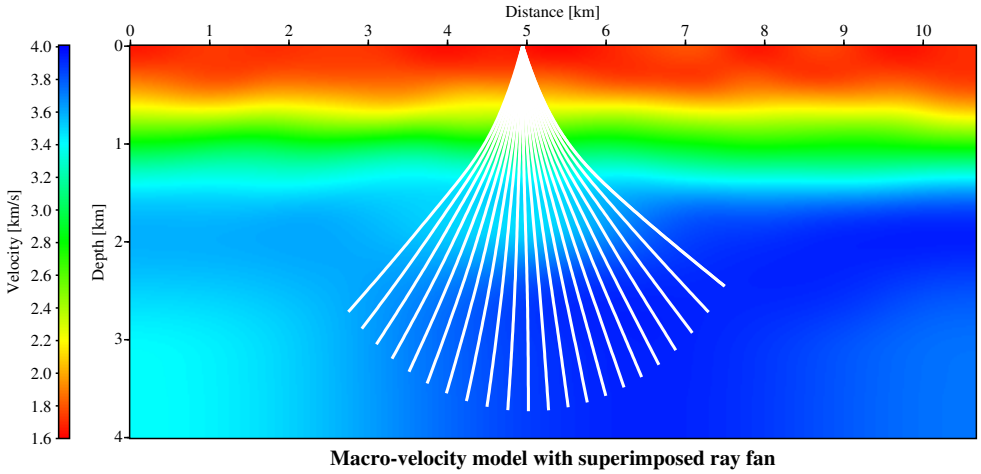

Figure 1: Macro-velocity model obtained by sequential application of CRS stack and NIP-wave inversion, here used for the model-based CDS stack. The attribute R_{CDS} has been calculated for all samples in the ZO target zone and emergence angles $-20^\circ \leq \alpha \leq 20^\circ$. For one emergence location, the ray paths for the coarse emergence angle grid are superimposed in white.

the CRS result in Figure 2a, the signal-to-noise ratio is slightly lower, but due to more complete and, thus, more physical stack section, this section is much better suited as input for poststack migration (Soleimani et al., 2009a,b). Finally, Figure 2c shows the very first result obtained with the data-driven CDS approach. For this section, all contributions for all considered emergence angles are simply superimposed, without any weighting or thresholding based on coherence. Whereas we observe even some more steep and/or strongly curved in the lower part, the result for the shallow part is quite unsatisfactory. The strong continuous reflection events in the CRS stack result appear much weaker here. We will discuss the probable reason for this effect below. In any case, the model-based CDS approach is significantly faster than its data-driven counterpart. Depending on the chosen parameters for the attribute search, the model-based approach is one to two orders of magnitude faster, although we additionally calculate semblance along the operators which is not required for this simple, unweighted and unthresholded kind of stack.

As mentioned in the preceding section, we calculate the semblance along each CDS operator in addition to the stack value. In this way, we can also keep track of the stacking parameters of the operator yielding the highest semblance value. This allows us to generate attribute pseudo sections—termed "pseudo", as they are not optimized in a data-driven way as in the CRS stack or the data-driven CDS stack, but obtained by forward-modeling. In Figure 3 the R_{CDS} pseudo section can be compared with the optimized and smoothed NIP wave radius section obtained from the CRS stack. Following the notation introduced above, the latter represents $R_{\mathrm{NIP,data}}$, whereas the CDS result represents $R_{\mathrm{NIP,mod}}$. At locations where the CRS attributes are determined in a stable manner, these two attributes should only differ by the aperture-dependent spread length bias. Indeed, both sections are very similar to each other, especially for the well-determined part up to about $1.8\,\mathrm{s}$. This result demonstrates that our forward-modeling in the CDS stack, the NIP-wave inversion, and the CRS stack itself are consistent with each other. Thus, we can be quite confident that the forward-modeling in the CDS approach is working properly.

Figure 4 compares the optimized and smoothed emergence angle section to the emergence angle pseudo section obtained by the model-based CDS approach. Although difficult to be seen, along some of the events both section almost coincide, indicating that the same events have been parameterized at the corresponding ZO locations. For the shallow part, the CDS result mainly shows a complicated pattern with quite large emergence angles. We interpret this a combination of an effect of spatial aliasing and aperture issues which will be discussed in more details below. Generally, the model-based CDS stack has for many ZO locations encountered the highest coherence for steep and/or strongly curved events which appear only as a few fragments in the CRS result. Generally, we expect that the CDS traveltime operator (2) will better fit diffraction events. This has been observed for the data-driven CDS approach and seems to be even more

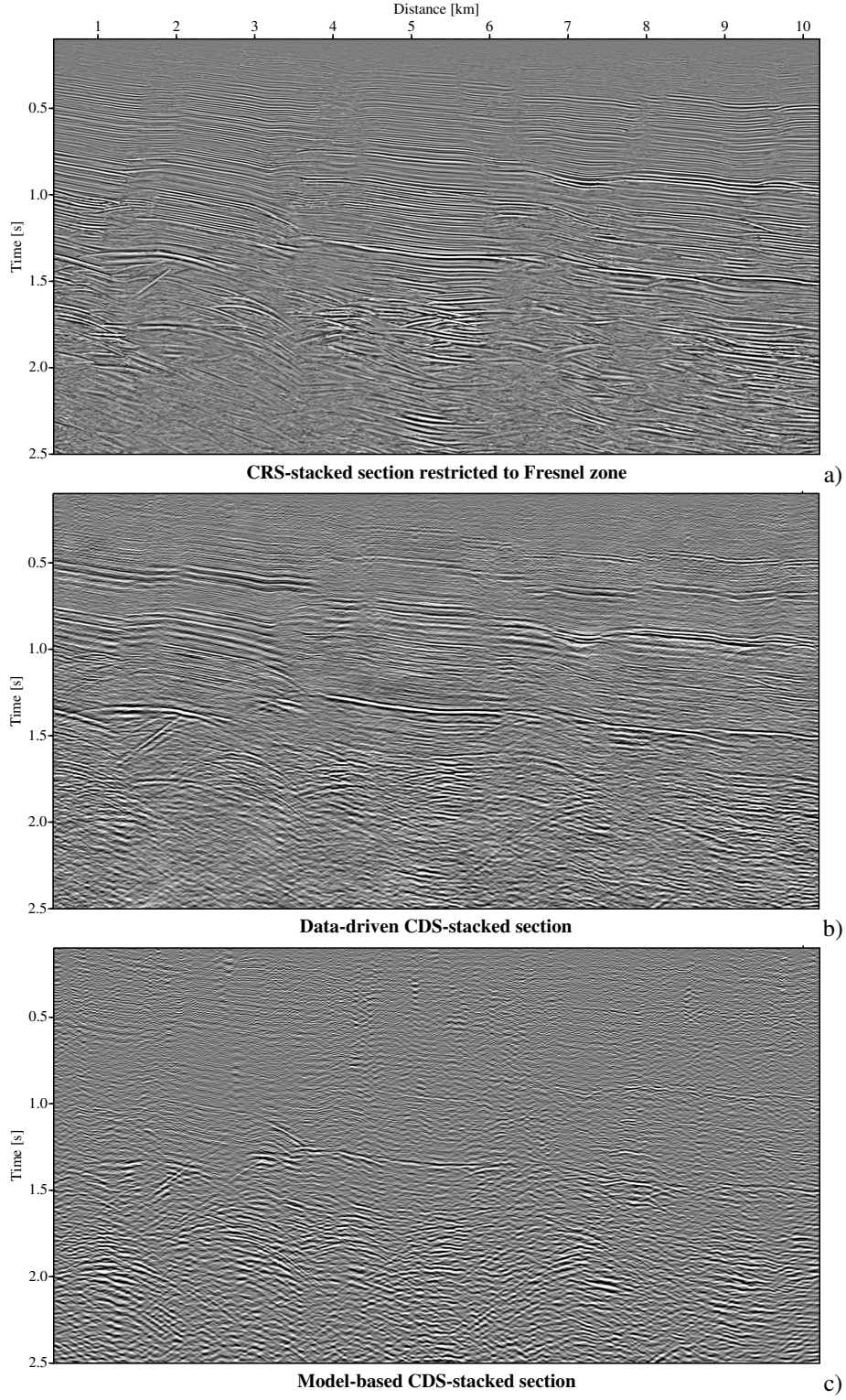

Figure 2: a) CRS-stacked section restricted to the projected first Fresnel zone. Note the artificial appearance with various truncated events. b) data-driven CDS-stacked section (modified after Soleimani et al., 2009a). The noise level is slightly increased, but the interference of intersecting events has been simulated everywhere. c) preliminary model-based counterpart generated in an significantly smaller computation time, without weighting suffering from spatial aliasing in the shallow part.

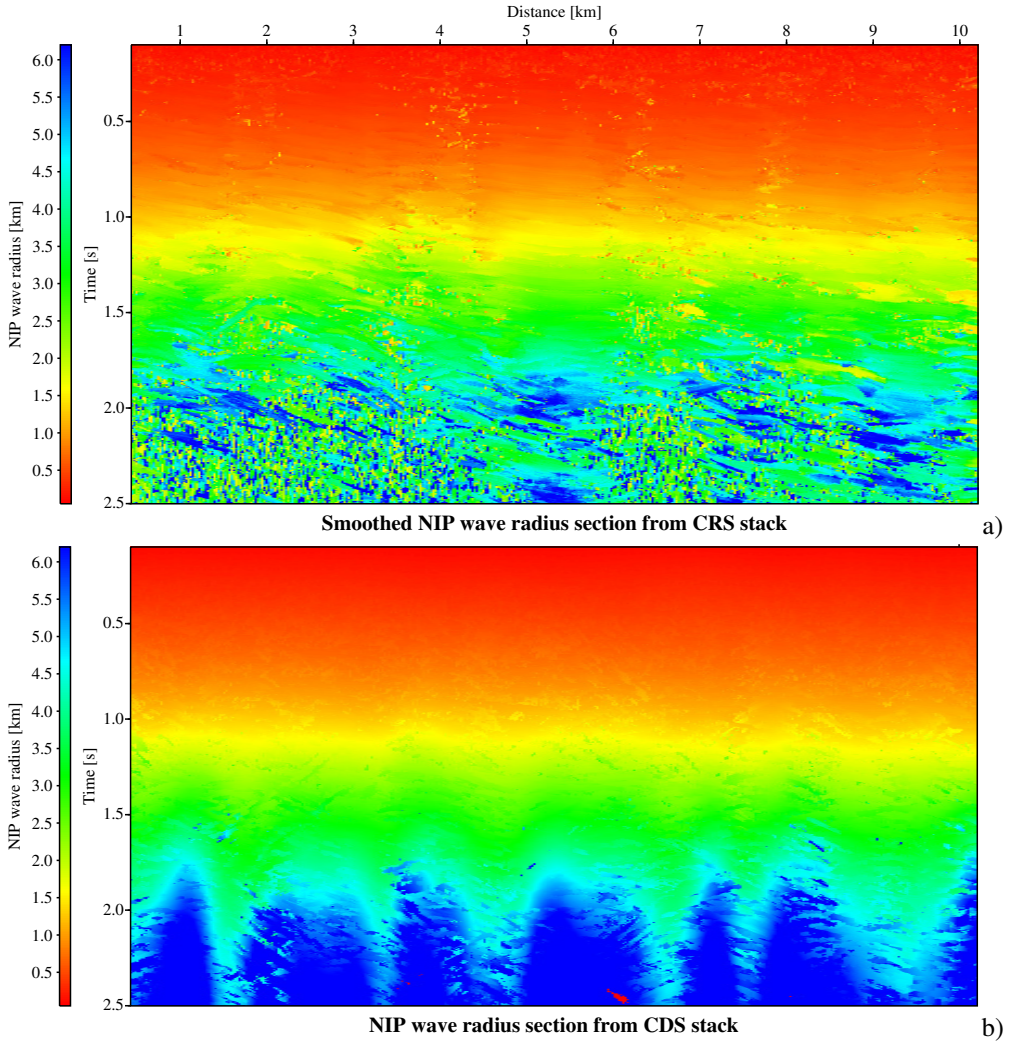

Figure 3: a) CRS-based NIP wave radius section after event consisting smoothing. b) CDS-based NIP wave radius pseudo section. The latter only shows the radius of curvature associated with the most coherent operator, whereas all operators for all angles contribute to the stack section in Figure 2. Note the extensive similarity of both sections.

pronounced in the model-based approach.

Finally, Figure 5 depicts the maximum coherence values encountered along the CRS operators or CDS operators, respectively. Note the different scales used in these figures. The CRS-based result shows very distinct reflection events with high coherence, but almost no indication of detected diffraction events. The vertical strips with relatively low coherence are associated with faults where lots of edge diffraction events complicate the wavefield. In contrast, the CDS-based result shows a completely different behavior: the overall semblance level is far lower and we mainly see diffraction events. These also show upon within the strips which are associated with low semblance values in the CRS result. The two section seem to complement each other—strong reflection events in the CRS result, lots of previously unseen diffraction events in the CDS result.

In summary, we observe a very distinct accentuation of diffraction events and a quite poor performance in the shallow region for the model-based CDS approach in this first application to real data. We attribute this behavior to the chosen midpoint aperture. The same aperture definition has been used for CRS stack, data-driven CDS stack, and model-based CDS stack. This aperture has been optimized for the CRS stack

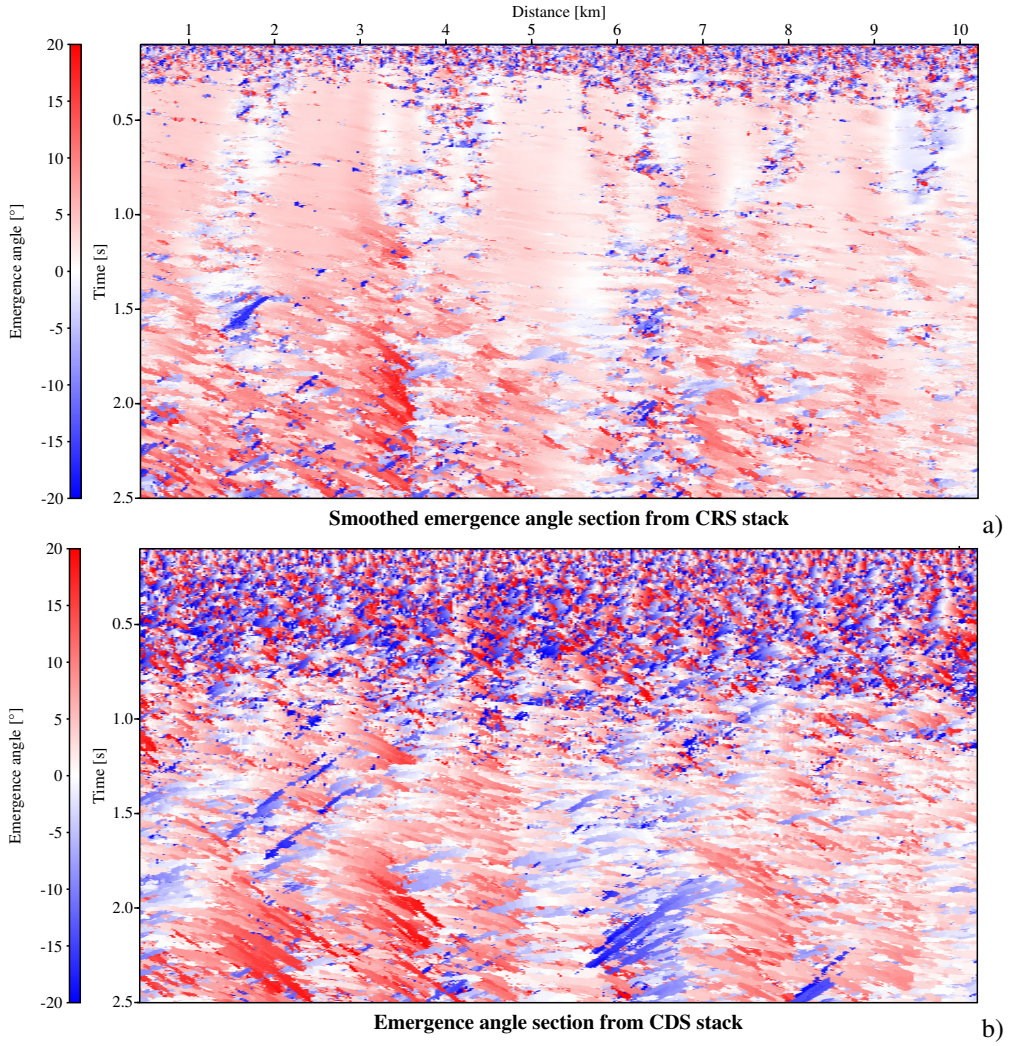

Figure 4: a) CRS-based emergence angle section after event consisting smoothing. b) CDS-based emergence angle pseudo section. At many locations, the latter parameterizes steeper events which are almost completely suppressed in the CRS result. Note that this section only shows the emergence angle associated with the most coherent operator, whereas all operators for all angles contribute to the stack section in Figure 2.

to allow a sufficiently stable determination of the normal wave radius of curvature R_{N}, which requires a sufficiently large aperture in midpoint direction. The CDS stacking operator (2) has one degree of freedom less and is, therefore, less accurate for reflection events. This applies in particular for concave reflection events for which the signs of R_{N} and R_{NIP} usually differ. Nevertheless, the data-driven CDS stack adapts to the reflection event as closely as possible and yields an operator which still fits reflection events reasonably. As mentioned above, R_{CDS} is a weighted average of the two wavefront radii in this case. However, for the model-based CDS approach, the situation is completely different. The forward-modeled radius of curvature does not at all depend on the reflector curvature or its time domain counterpart R_{N}, such that the corresponding operator very poorly approximates the reflection event for a larger midpoint displacement, whereas the fit in the vicinity of the central CMP gather should be very good. The smaller the ZO traveltime, the larger usually the relative difference between the two radii R_{N} and R_{NIP}, i. e., the fit in midpoint direction gets even worse. This explains the poor performance at shallow times. In contrast, for diffraction events, $R_{\mathrm{N}} \approx R_{\mathrm{NIP}}$, thus they are well imaged even within a large midpoint aperture and/or for small ZO

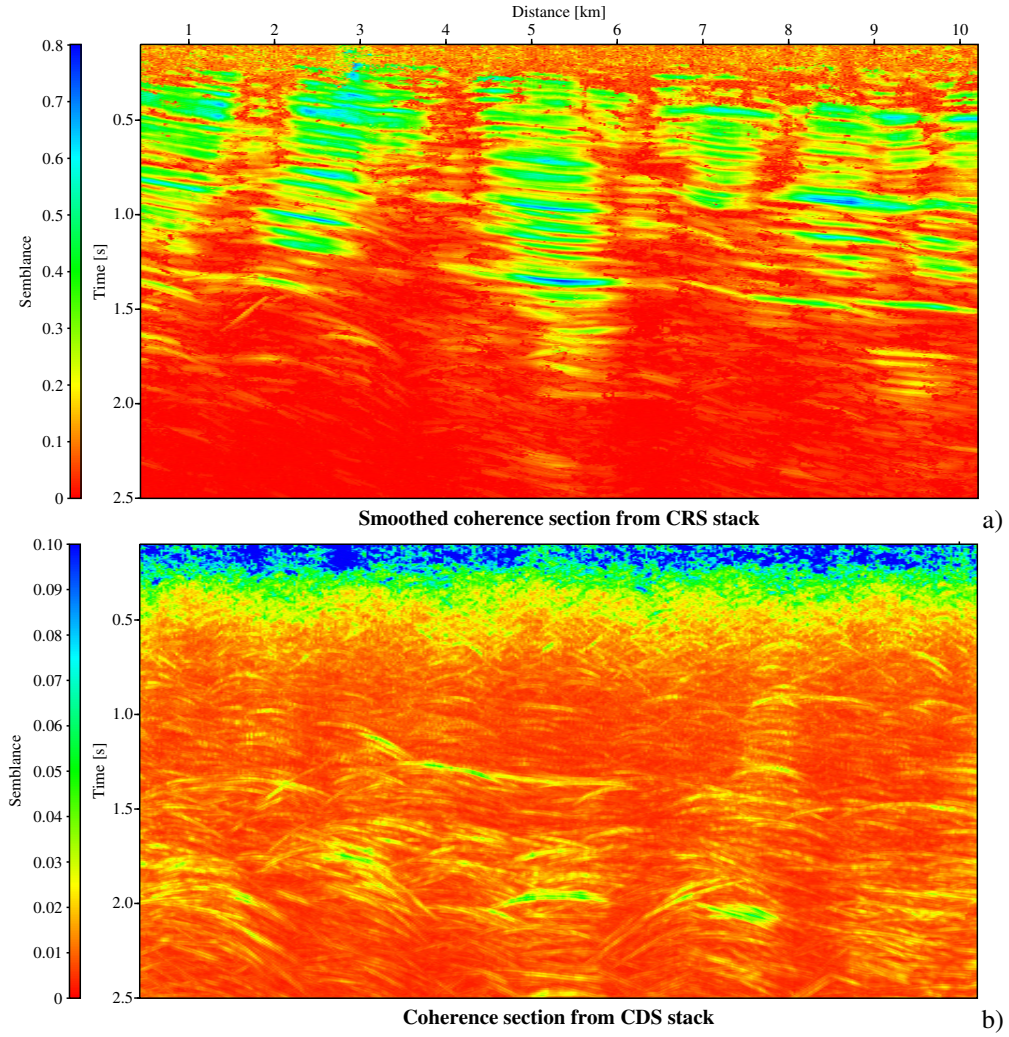

Figure 5: a) CRS-based coherence section after event consisting smoothing. b) CDS-based coherence pseudo section. Note the different scaling of both plots. The overall coherence in the latter is significantly lower and mainly shows those curved events (mainly diffractions) which are missing in the CRS-based result. Again, the CDS section only shows the semblance value associated with the most coherent operator, whereas all operators for all angles contribute to the stack section in Figure 2.

times. In our future research, we will investigate the use of smaller midpoint apertures, probably totally detached from the aperture definitions currently used in the CRS stack. One promising option is to attach a narrow aperture to the approximation of the common-reflection-point trajectory discussed by Höcht et al. (1999). Along this trajectory, the influence of R_{N} is negligible.

CONCLUSIONS AND OUTLOOK

We have implemented and tentatively applied a model-based approach to the CDS stack method. This is intended to fully resolve the conflicting dip problem occurring in complex data and, thus, to allow to simulate a complete stacked section containing all mutually interfering reflection and/or diffraction events. In contrast to the entirely data-driven CDS method, this model-based approach is far more efficient. The required macro-velocity model can be generated with any established method, including the the sequential application of CRS stack and NIP-wave tomography. The model-based CDS stack is tailored to optimize the stacked section for a subsequent poststack depth migration. This is relevant for situations in which

the generation of velocity models sufficiently accurate for prestack depth migration is difficult or even impossible.

The first results indicate that further investigation are required to assess the appropriate choice of adequate apertures for the model-based CDS stack. With the current aperture choice according to the needs of the CRS stack, the process acts as a strong filter for diffraction events, a feature which might be very helpful to delineate discontinuities in the subsurface. With smaller aperture, we expect a joint image of reflection and diffraction events. The additional use of the coherence as weight factor or criterion to accept or reject the contribution of a particular CDS operator to decrease the noise level will also be investigated.

ACKNOWLEDGMENTS

This work was kindly supported by the sponsors of the *Wave Inversion Technology (WIT) Consortium*, Hamburg, Germany. H. Shahsavani acknowledges the support of the *Ministry of Science, Research and Technology*, Iran.

REFERENCES

Červený, V. (2001). *Seismic ray theory*. Cambridge University Press, Cambridge.

Duveneck, E. (2004a). 3D tomographic velocity model estimation with kinematic wavefield attributes. *Geophys. Prosp.*, 52(6):535–545.

Duveneck, E. (2004b). Velocity model estimation with data-derived wavefront attributes. *Geophysics*, 69(1):265–274.

Hale, D. (1991). *Dip Moveout Processing*. Soc. Expl. Geophys., Tulsa.

Heilmann, Z., Mann, J., Duveneck, E., and Hertweck, T. (2004). CRS-stack-based seismic reflection imaging – a real data example. In *Extended abstracts, 66th Conf.* Eur. Assn. Geosci. Eng. Session P211.

Hertweck, T., Jäger, C., Mann, J., Duveneck, E., and Heilmann, Z. (2004). A seismic reflection imaging workflow based on the Common-Reflection-Surface (CRS) stack: theoretical background and case study. In *Expanded Abstracts, 74th Ann. Internat. Mtg.* Soc. Expl. Geophys. Session SP 4.3.

Hertweck, T., Mann, J., and Klüver, T. (2005). Event-consistent smoothing in the context of the CRS stack method. *J. Seis. Expl.*, 14(2-3):197–215.

Hertweck, T., Schleicher, J., and Mann, J. (2007). Data-stacking beyond CMP. *The Leading Edge*, 26(7):818–827.

Höcht, G., de Bazelaire, E., Majer, P., and Hubral, P. (1999). Seismics and optics: hyperbolae and curvatures. *J. Appl. Geophys.*, 42(3,4):261–281.

Jäger, R., Mann, J., Höcht, G., and Hubral, P. (2001). Common-Reflection-Surface stack: image and attributes. *Geophysics*, 66(1):97–109.

Mann, J. (2001). Common-Reflection-Surface stack and conflicting dips. In *Extended abstracts, 63rd Conf.* Eur. Assn. Geosci. Eng. Session P077.

Mann, J. (2002). *Extensions and applications of the Common-Reflection-Surface Stack method*. Logos Verlag, Berlin.

Mann, J., Duveneck, E., Hertweck, T., and Jäger, C. (2003). A seismic reflection imaging workflow based on the Common-Reflection-Surface stack. *J. Seis. Expl.*, 12(3):283–295.

Mann, J., Jäger, R., Müller, T., Höcht, G., and Hubral, P. (1999). Common-Reflection-Surface stack – a real data example. *J. Appl. Geophys.*, 42(3,4):301–318.

Müller, N.-A. (2006). Elimination of the spread-length bias in the Common-Reflection-Surface stack. In *Expanded Abstracts, 76th Ann. Internat. Mtg.*, pages 3006–3010. Soc. Expl. Geophys.

Soleimani, M., Mann, J., Adibi Sedeh, E., and Piruz, I. (2010). Improving the seismic image quality in semi-complex structures in North East Iran by the CDS stack method. In *Extended abstracts, 72nd Conf.* Eur. Assn. Geosci. Eng. Session P398.

Soleimani, M., Piruz, I., Mann, J., and Hubral, P. (2009a). Common-Reflection-Surface stack: accounting for conflicting dip situations by considering all possible dips. *J. Seis. Expl.*, 18(3):271–288.

Soleimani, M., Piruz, I., Mann, J., and Hubral, P. (2009b). Solving the problem of conflicting dips in Common-Reflection-Surface stack. In *Extended Abstracts, 1st Internat. Conf. & Exhib., Shiraz, Iran*. Eur. Assn. Geosci. Eng.